PAKAL: A THREE-DIMENSIONAL MODEL TO SOLVE THE RADIATIVE TRANSFER EQUATION

Victor De la Luz[1], Alejandro Lara[1], J. E. Mendoza-Torres[2], and Caius L. Selhorst[3,4]
[1] Instituto de Geofísica, Universidad Nacional Autónoma de México, 04510, Mexico
[2] Coordinación de Astrofísica, Instituto Nacional de Astrofísica Óptica y Electrónica, 72840, Mexico
[3] CRAAM, Universidade Presbiteriana Mackenzie, São Paulo, SP 01302-907, Brazil
[4] IP&D, Universidade do Vale do Paraíba, São José dos Campos, SP 01302-907, Brazil

ABSTRACT

We present a new numerical model called "Pakal" intended to solve the radiative transfer equation in a three-dimensional (3D) geometry, using the approximation for a locally plane-parallel atmosphere. Pakal uses pre-calculated radial profiles of density and temperature (based on hydrostatic, hydrodynamic, or MHD models) to compute the emission from 3D source structures with high spatial resolution. Then, Pakal solves the radiative transfer equation in a set of (3D) ray paths, going from the source to the observer. Pakal uses a new algorithm to compute the radiative transfer equation by using an intelligent system consisting of three structures: a cellular automaton; an expert system; and a program coordinator. The code outputs can be either two-dimensional maps or one-dimensional profiles, which reproduce the observations with high accuracy, giving detailed physical information about the environment where the radiation was generated and/or transmitted. We present the model applied to a 3D solar radial geometry, assuming a locally plane-parallel atmosphere, and thermal free–free radio emission from hydrogen–helium gas in thermodynamic equilibrium. We also present the convergence test of the code. We computed the synthetic spectrum of the centimetric–millimetric solar emission and found better agreement with observations (up to 10^4 K at 20 GHz) than previous models reported in the literature. The stability and convergence test show the high accuracy of the code. Finally, Pakal can improve the integration time by up to an order of magnitude compared against linear integration codes.

Key words: methods: numerical – radiation mechanisms: thermal – radiative transfer – Sun: atmosphere – Sun: chromosphere – Sun: radio radiation

Online-only material: color figures

1. INTRODUCTION

The observation and study of radio emissions coming from distant sources are valuable tools to investigate these objects and the medium between them and the observer. For instance, by assuming an emission mechanism, we are able to obtain detailed physical properties of the observed object as density, temperature, magnetic field, etc.

Generally, due to observational limitations, we obtain two-dimensional (2D) projections in the plane of the sky of the emission and/or absorption in the ray paths of each point of the observed region inside the telescope field of view. These maps represent not only the emitting object, but also all the possible flux changes due to the emission and/or absorption that may take place in the medium between the source and the observer. Therefore, to get reliable information through the study of radio emissions, it is necessary to take into account the detailed three-dimensional (3D) structure of both the source and the medium. In this work, we present "Pakal," a numerical model intended to solve the radiative transfer equation, designed to study astronomical objects in the millimeter and submillimeter wavelengths.

Nowadays, there are a few dozen of codes to solve the radiative transfer equation, though each code is designed to solve a very specific problem. For instance, there are codes to solve the radiative transfer equation in Earth-like atmospheres (e.g., Oreopoulos et al. 2006; Cahalan et al. 2005; Davis & Cahalan 2001). More specifically, the I3RC Monte Carlo community model of 3D radiative transfer (Cahalan et al. 2005), the ARTS package (Buehler et al. 2005), the Battaglia–Mantovani model

(Battaglia & Mantovani 2005), GRIMALDI (Scheirer & Macke 2001), MCARaTS (Iwabuchi 2006), SHDOM (Evans 1998), and SHARM-3D (Lyapustin 2002) are designed to study the dispersion of telecommunication radio waves in the Earth atmosphere. These models simulate layers of a plane-parallel atmosphere and are based mainly on Monte Carlo techniques.

In the astrophysics community, there are mainly two branches of codes to simulate the emission of stellar atmospheres.

1. Codes to simulate the atmosphere structure (the variation with height of physical parameters as density, temperature, etc.).
2. Codes to compute the synthetic spectrum.

Commonly, the codes for stellar atmosphere simulation deal with specific physical conditions. For example, ATLAS12 (Kurucz 1979), MARCS (Gustafsson et al. 1975), and PHOENIX (Hauschildt et al. 1999) are general propose codes for stellar atmospheres which take into account only the emissions from the stellar photospheres. The PANDORA (Vernazza et al. 1976) and MULTI (Carlsson 1992) codes simulate stellar atmospheres using conditions similar to the solar atmosphere but only in the region below the corona, whereas CHANTI (Dere et al. 1997) simulates atmospheres with coronal conditions. The chromospheric and coronal codes are oriented to reproduce the ultraviolet (UV) and visible spectra, and therefore fail to reproduce observations in the radio range (Zirin et al. 1991; Ewell et al. 1993; Selhorst et al. 2005).

Examples of codes in the second branch (synthetic radiative spectrum) are SYNTHE (Kurucz 1979), SPECTRUM (Hubeny & Lanz 1995), and FANTOM (Cayrel et al. 1991). These codes

are complementary to codes in the former branch and are necessary to compute the final stellar spectrum. We note that PANDORA and CHANTI, from the first group, are also able to compute the spectrum.

Some codes are intended to compute particular stellar atmospheres, e.g., STERNE3 (Behara & Jeffery 2006) for hydrogen-deficient stars; LINE-BY-LINE METHOD (Shulyak et al. 2004) for stars in early and intermediate stages; PRO2 (Werner 1986) and TLUSTY (Hubeny & Lanz 1995) for hot stars; WM-basic (Pauldrach et al. 2001) for expanding atmospheres; CMFGEN (Hillier & Miller 1998) for Wolf–Rayet stars; and FASTWIND (Santolaya-Rey et al. 1997) for stars with high mass loss.

Pakal is a completely new code that can be applied to any geometry, radiation, and absorption mechanism (focused in this work to millimeter and submillimeter wavelengths, but easily configurable for other wavelengths). This flexibility is achieved by the means of four completely independent modules: the numerical model (Section 2), the geometry model (Section 3.2), numerical methods, and physical functions (Section 3.3).

Pakal uses a new method to compute the radiative transfer equation in a set of 3D ray paths; this is an intelligent system called "Tulum" (Section 3.1) which helps to reduce the integration time up to 1 order of magnitude as compared with direct integration codes (Section 4). Pakal is able to compute the contributions to the opacity function of each chemical element and its ionization states. To accomplish this, the code needs, as input, detailed profiles of electron temperature and ion densities (Appendix A).

2. RADIATIVE TRANSFER THEORY

The specific intensity is the most basic entity in radiative transfer theory and is defined as the amount of energy dE passing though an area dA, during a time dt, coming inside a solid angle dw, in an interval of frequency $d\nu$, with a direction given by $\hat{r}$ (Rohlfs 1986):

$$dI_\nu = \frac{dE}{dA\, dt\, dw\, d\nu\, \hat{r} \cdot \hat{n}},$$

where $\hat{r}$ and $\hat{n}$ are the direction and normal (to dA) unitary vectors, respectively, and can be written as

$$\hat{r} \cdot \hat{n} = \cos\theta = \mu,$$

where θ is the angle between $\hat{r}$ and $\hat{n}$. When radiation interacts with matter, crossing a distance ds, the change in the specific intensity dI_ν is equal to the emission of the medium, ϵ_ν, minus the radiative energy absorbed by the medium, $\kappa_\nu I_\nu$; this is (Chandrasekhar 1960)

$$\frac{dI_\nu}{ds} = -\kappa_\nu I_\nu + \epsilon_\nu, \qquad (1)$$

where κ_ν is the opacity function which depends on the physical properties of the medium. Assuming a plane-parallel atmosphere, it is possible to write ds in terms of the geometric distance dx (see Figure 1):

$$dx = ds\cos(\theta) = \mu\, ds,$$

then using the optical depth, $d\tau_\nu = -\kappa_\nu\, dx$, and Kirchhoff's law ($\epsilon_\nu = \kappa_\nu S_\nu$), Equation (1) may be written as

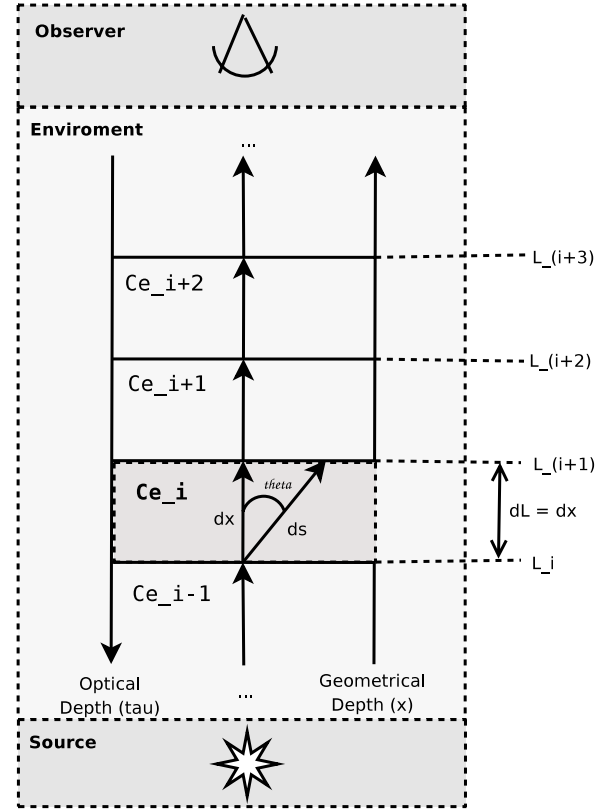$$\frac{dI_\nu}{d\tau_\nu} - \frac{I_\nu}{\mu} = -\frac{S_\nu}{\mu}.$$

Figure 1. General geometry used in the numerical model.

The solution in the $[\tau_{1,\nu},\, \tau_{2,\nu}]$ optical depth interval (where $\tau_{1,\nu} > \tau_{2,\nu}$) is

$$I_\nu(\tau_{2,\nu}) = I_\nu(\tau_{1,\nu})\, e^{-(\tau_{1,\nu}-\tau_{2,\nu})/\mu}$$
$$- \frac{1}{\mu}\int_{\tau_{1,\nu}}^{\tau_{2,\nu}} S_\nu(\tau_\nu) e^{-(\tau_\nu - \tau_{2,\nu})/\mu} d\tau_\nu. \qquad (2)$$

For solar conditions, the scattering is negligible in the millimeter and submillimeter wavelength range (Vernazza et al. 1976). Therefore, for our purposes Equation (2) is completely valid.

Assuming $\tau_2 < \tau_1$; $\mu = 1$ and a source function constant in each cell "i" ($0 \leqslant i \leqslant n$), we integrate Equation (2) in an array of n consecutive cells (see Figure 1), using

$$I_\nu(L_{i+1}) = I_\nu(L_i)\exp\left[-\frac{dL}{2}(k_\nu(L_i) + k_\nu(L_{i+1}))\right]$$
$$+ S_\nu(L_i + 0.5\, dL)\left(1 - \exp\left[-\frac{dL}{2}(k_\nu(L_i) + k_\nu(L_{i+1}))\right]\right), \qquad (3)$$

where $I(L_i)$ is the specific intensity (coming) from the cell "$i-1$"; $I(L_{i+1})$ is the specific intensity (getting out) of the cell "i"; and dL is the integration step. The computation of each L_i is done by the geometry module (see Section 3.2).

3. PAKAL MODEL

Pakal (the name of the king of Palenque in the Mayan Culture) is written in C language, using an object-oriented technique (Schildt 1987) which allows us to encapsulate sets of common properties or functions in libraries. The code is based
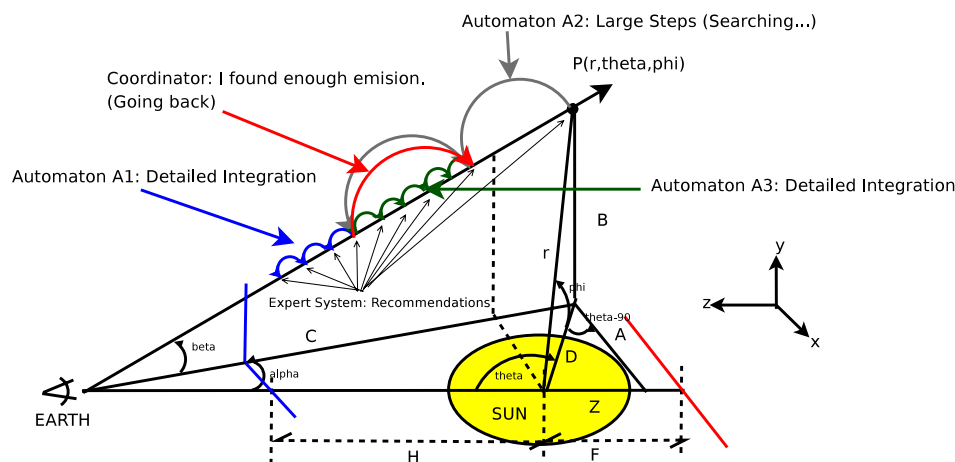
Figure 2. Detailed geometry used in Pakal showing, in an (Earth–P) ray path, three possible states of the integration process.
(A color version of this figure is available in the online journal.)

on four independent modules: (1) the numerical model, (2) the geometry, (3) numerical methods, and (4) physical functions.

Once the geometry is defined, Pakal generates a series of independent ray paths, from the source to the observer, reads pre-defined temperature and density profiles, and, if necessary, performs an interpolation of the read values, covering a larger number of points in altitude. Then, using an intelligent system called Tulum, solves the radiative transfer equation (the related algorithms are part of the numerical module).

3.1. Tulum: The Intelligent System

The intelligent system used in Pakal is called Tulum and helps to solve the radiative transfer equation in a new and very efficient way. In Figure 2, a schematic diagram of the automaton is presented.

Tulum is formed by the following three independent components.

1. A coordinator which controls each step of the integration process. The coordinator uses the recommendations of the expert system and the states of the cellular automaton to decide the next stage of the integration process.
2. An expert system who recommends, based on the current status (position and physical conditions), whether or not it is necessary to integrate in this point and, if necessary, recommends a change of the integration step size.
3. A cellular automaton, with a set of previously established states, which is able to save the current status of the integration process.

Tulum can numerically integrate any given function (not only the radiative transfer equation). The integration process is carried out in the following way.

1. When the coordinator program receives the spatial coordinates of two contiguous integration points (from the 3D geometry module), it looks for the physical conditions at these points (from the temperature and density radial models). If necessary, the numerical module of Pakal automatically interpolates the radial temperature and density models, at the specific points, using either of the two classical methods: linear or cubic spline interpolations. In this work, we use linear interpolation (the cubic spline interpolation fails because the temperature profile has a very large gradient in the solar transition zone).

Once the coordinator knows the physical conditions of the medium, he asks for a recommendation to the expert system and also for the present state of the cellular automaton. Based on this information, the coordinator can take the decision of either going ahead with the integration process (using small or large steps) or going backward. Then, the coordinator computes the emission (using the numerical module; see Section 3.3) and updates the current state of the automaton via the ϵ variable (which is used to switch between two automaton states).

The set of possible decisions (as shown in Table 1) are based on two considerations:

a) In order to save computation time, we neglect the emission that does not contribute to the total brightness temperature.
b) On the other hand, we include, with a high spatial resolution, the emission of any structure in the solar atmosphere, which contributes to the total brightness temperature.

2. The second component is the expert system which, based on the physical conditions of each specific point, decides if it is useful to integrate on this region and recommends the size of the following integration step. The recommendation is based on two plasma parameters: the plasma frequency ($\nu_p = 9 \times 10^{-3} \sqrt{n_e}$ (MHz)) and the minimal emission.

The plasma frequency is important to obtain the position (atmospheric height) of the interface between regions where electromagnetic waves, at any given frequency, can propagate or not.

The minimal emission parameter defines the lower limit where the local emission is negligible and also controls both, the error due to this neglected flux and the performance of the integration process, saving in this way a large amount of computation time. There is also another numerical error, associated with the small and large steps. We present the analysis of convergence of these errors in Appendix B. The minimal emission can be set by the user via the "-min" parameter at the console or can be managed automatically by the code (see Section 3.4).

The expert system can recommend the integration steps (small or large) based on the following cases.

a) If $\nu_p > \nu$, then the wave cannot propagate and the expert recommends a small integration step. We

consider this case, because we want to know the height where the radiation starts propagating in the atmosphere.

   b) If $v_p \leqslant v$, and the local emission is greater than the minimal emission (the amount of emission is important). The wave can propagate and the expert recommends small integration step (we want to analyze in detail the emission process).

   c) If $v_p \leqslant v$, and the local emission is lower than the minimal emission, the wave can propagate but there is not enough emission; therefore, the expert recommends a large integration step (we want to save time in the computation process).

The recommendations are managed by two variables: "q," the local behavior of the emission and "y," the size of the integration step (see Table 2). These variables are transmitted to the coordinator as well as the variable "state" which contains the current state of the cellular automaton (Table 1).

3. The cellular automaton is the logical structure that stores the stage of the integration process, and represents the memory of the system. It is controlled by two parameters: ϵ (the variable that preserves the memory when the system switches from one state to another) and the stack, a logical structure which preserves a local memory of the automaton states. The stack helps us to control the number of steps when the coordinator decides to "go back" in the integration process and is represented by two integer variables: "i" and "n" (where n = large step/small step; in this way, we guarantee that the total length of the small and large steps is the same when the system enters into the "go back" process).

The automaton can be in any of the four following states (see Table 3).

   a) A1: integrating using small steps.

   b) A2: integrating using large steps.

   c) A3: "going back": I tried to integrate using large steps but I had to return because the local emission is larger than the minimal emission. Therefore, I will integrate with small steps up to the returning point (this state shows the necessity of the stack structure).

   d) A4: something is wrong. This is an error.

In summary, the three components of Tulum perform a very efficient intelligent system to switch between integration steps; control the associated errors and reproduce the emission with high spatial resolution.

3.2. 3D Geometrical Model

The geometrical model was designed to optimize the computations of solar 3D structures based on radial profiles of physical parameters (in general, quiet-Sun models for the electronic density and temperature are given as radial profiles, starting at photospheric level and extending to different atmospheric altitudes).

The origin of the coordinated system is located at the center of the solar sphere, the Z-axis points toward the observer, the Y-axis points to the solar north, and the X-axis completes the system. In this geometry, a ray path from a given point in the plane of the sky to the observer is formed by a set of radial vectors (see Figure 2). These vectors describe both the integration mesh and the radial values of density and temperature along this ray path. The radiative transfer equation is integrated along each ray path

Table 1
Decision Table of the Coordinator

State	q	y	Instructions	ϵ	Step (dz)
A1	0	0	$I = 0$	0	Small
			$x_a = x_b$		
			$x_a + = dzdetail$		
	1	1	$x_a = x_b$	1	Large
			$x_a + = dz\,big$		
	2	0	$I = I_o e^{-\tau} + S(1 - e^{-\tau})$	0	Small
			$x_a = x_b$		
			$x_b + = dzdetail$		
A2	0	0	$I = 0$	0	Small
			$x_a = x_b$		
			$x_b + = dzdetail$		
	1	1	$x_a = x_b$	1	Large
			$x_b + = dz\,big$		
	2	0	$x_b = x_a + dzdetail$	2	Small
A3	0	0	$I = 0$	0	Small
			$x_a = x_b$		
			$x_b + = dzdetail$		
	1	1	$I = I_o e^{-\tau} + S(1 - e^{-\tau})$	1	Small
			$x_a = x_b$		
			$x_b + = dzdetail$		
	2	0	$I = I_o e^{-\tau} + S(1 - e^{-\tau})$	1	Small
			$x_a = x_b$		
			$x_b + = dzdetail$		

Notes. I is the local emission after the computation; I_o is the incoming emission; S is the source function; τ is the local opacity; x_a and x_b are the two spatial coordinates; $dzdetail$ is the small integration step; and $dzbig$ is the large integration step. Using this decision table, the coordinator chooses the integration step and computes the local emission I.

Table 2
State of the Expert System, Where q and y are the Possible Recommendations

Variable	Value	Meaning
y	0	Next step small
	1	Next step large
	2	Next step backward
q	0	The wave cannot propagate
	1	The emission is not enough
	2	There is enough emission

and the set of ray paths forms the 2D projection (on the plane XY) of the 3D model.

In this geometry, each point of the mesh is defined as

$$\vec{r}_{\alpha_x, \beta_y}(z) = (r(\alpha_x, \beta_y, z), \theta(\alpha_x, \beta_y, z), \phi(\alpha_x, \beta_y, z)),$$

where r is the module of vector $\vec{r}$, θ is the angle between the Z-axis and the projection of $\vec{r}$ on the XZ plane, ϕ is the angle between $\vec{r}$ and the ZY plane, and z is the projection of $\vec{r}$ onto the Z-axis. From the observer's point of view, each ray path represents a pixel (x, y) on the projected 2D image and is defined by the angles α_x and β_y. Each ray path is divided into k points separated by a distance dl; for simplicity, we do not use directly dl but its projection, dz, on the Z-axis.

The mesh is defined by two constants: the astronomical unit, $AU = 1.5 \times 10^8$ km and the solar radii $R_\odot = 6.96 \times 10^5$ km; plus the following variables.

Table 3
Table of States of the Cellular Automaton

State	ϵ	New State	Execute
A1	0	A1	Nothing
	1	A2	Nothing
	2	A4	Nothing
A2	0	A1	Nothing
	1	A2	Nothing
	2	A3	$i = 1$
A3	0	A1	Nothing
	1 AND ($i < n$)	A3	i++
	1 AND ($i = n$)	A1	Nothing
	2	A4	Nothing
A4	0	Null	Error
	1	Null	Error
	2	Null	Error

Notes. In this case, $n = dzbig/dzdetail$. The variable "state" represents the memory stages of the integration process; "ϵ" controls the switch between states; and the variable "i" is a stack into the automaton.

1. n: the image resolution is $n \times n$ pixels.
2. x: variable in the X-direction ranging from $-(n-1)/2$ to $(n-1)/2$.
3. y: variable in the Y-direction ranging from $-(n-1)/2$ to $(n-1)/2$.
4. R_T: the maximum radial distance, in the 2D projection, considered for the integration (we use $R_T = 2\,R_\odot$).
5. F defines (in units of solar radii) the starting point of the integration process, $F = 0$ means that the starting point lies in the plane XY; $F = -1$ in a parallel plane located at one solar radii behind of the origin; and $F = 1$ in a parallel plane located at one solar radii in front of the origin (by default, we use $F = -R_T$).
6. H is the final point of the integration process; the default value is $H = R_T$.
7. dl: integration step in km.

The process starts by computing the matrix of angles:

$$M_{n,n} = \left\{ (\alpha(x), \beta(y)) \mid \frac{-(n-1)}{2} \leqslant x, y \leqslant \frac{n-1}{2} \right\}.$$

Then, the initial and final integration points are computed for each element $M_{x,y}$. These points are defined by the user (F and H, respectively). It is possible that some ray paths intersect the solar surface; for such cases, we define $F = z_0$, where z_0 is the projection of the intersection point on the Z-axis. Once the initial and final integration points are known, the code generates the set of points:

$$L_{x,y} = \{r(\alpha_x, \beta_y, z), \theta(\alpha_x, \beta_y, z), \phi(\alpha_x, \beta_y, z) \mid z_0 \leqslant z \leqslant H$$
$$\text{and } z = m * dz, m \in N\},$$

and solve Equation (3).

3.3. Model for Thermal Radio Emission

At quiet regions, the main contribution to the emission and absorption is due to free–free interactions, in particular, free electrons interacting with ions. The electron–electron, ion–ion, and free–bound interactions do not contribute significantly to the total emission (Dulk 1985). Even more, for radio emissions,

only distant electron–ion interactions are important (Dulk 1985). Therefore, in this case, the absorption coefficient is (Dulk 1985)

$$\kappa_\nu = \sum_i \frac{1}{3c} \left(\frac{2}{\pi}\right)^{1/2} \frac{\nu_p^2}{\nu^2} \frac{4\pi Z_i^2 n_i e^4}{m^{1/2}(kT^{3/2})} \frac{\pi}{\sqrt{3}} G(T, \nu), \quad (4)$$

where n_i is computed using the Saha equation (Athay & Thomas 1961):

$$\log \frac{n_{i+1}}{n_i} = -0.1761 - \log(P_e) + \log \frac{u_{i+1}}{u_i}$$
$$+ 2.5 \log T - \chi_i \frac{5040}{T}, \quad (5)$$

where u_i is the statistical weight, χ_i is the ionization energy, $P_e = n_e KT$, and n_e is the observed electronic density profile.

Equation (4) may be approximated, according to the appropriate Gaunt factor, to

$$\kappa_\nu \approx 9.78 \times 10^{-3} \frac{n_e}{\nu^2 T^{3/2}} \sum_i Z_i^2 n_i$$
$$\times \begin{cases} 18.2 + \ln(T^{3/2}) - \ln \nu, & T < 2 \times 10^5 \text{ K} \\ 24.5 + \ln(T) - \ln \nu, & T > 2 \times 10^5 \text{ K}. \end{cases} \quad (6)$$

The source function is

$$I_\nu = \frac{2h\nu^3}{c^2} \frac{1}{\exp(h\nu/kT) - 1}. \quad (7)$$

Although, at radio wavelengths $h\nu \ll kT$, it is possible to use the Rayleigh–Jeans approximation:

$$I_\nu \approx \frac{2k\nu^2}{c^2} T. \quad (8)$$

Equations (6) and (8) are solved by our model. We have simulated the solar emission in the radio wavelength range and found a good agreement with observations (Section 4).

3.4. The Minimal Emission Parameter

As shown in the upper panel of Figure 3, where we have plotted the total emission as a function of the photospheric height for different frequencies, from 7 GHz (black curve) to 7 THz (blue curve), above 3000 km the total emission has reached its final value for all frequencies. Obviously, this convergence occurs at different heights depending on the frequency, and the minimum height of convergence ($\sim$590 km, marked with a vertical dotted line) corresponds to the 7 THz profile. We use this point as a reference height (h_c).

On the central panel of Figure 3, we have plotted the "emission efficiency,"

$$I_{\text{eff}} = 1 - \exp(-\tau_\nu(z)),$$

as a function of height for the same frequency range. Clearly, the 7 THz profile has the lowest "emission efficiency" at all heights. Therefore, we can use the value of the "emission efficiency" of this profile at h_c, that is, $I_{\text{eff}} = 1 \times 10^{-4}$, as the lower bound of the model (marked with a horizontal dotted line). The "emission efficiency" can reach lower values; at higher altitudes, but as seen in the upper panel, the contribution to the total emission (for the 7 THz profile) at these heights is negligible.

As we do not know, before the computations, where the "emission efficiency" will reach this lower bound value, we
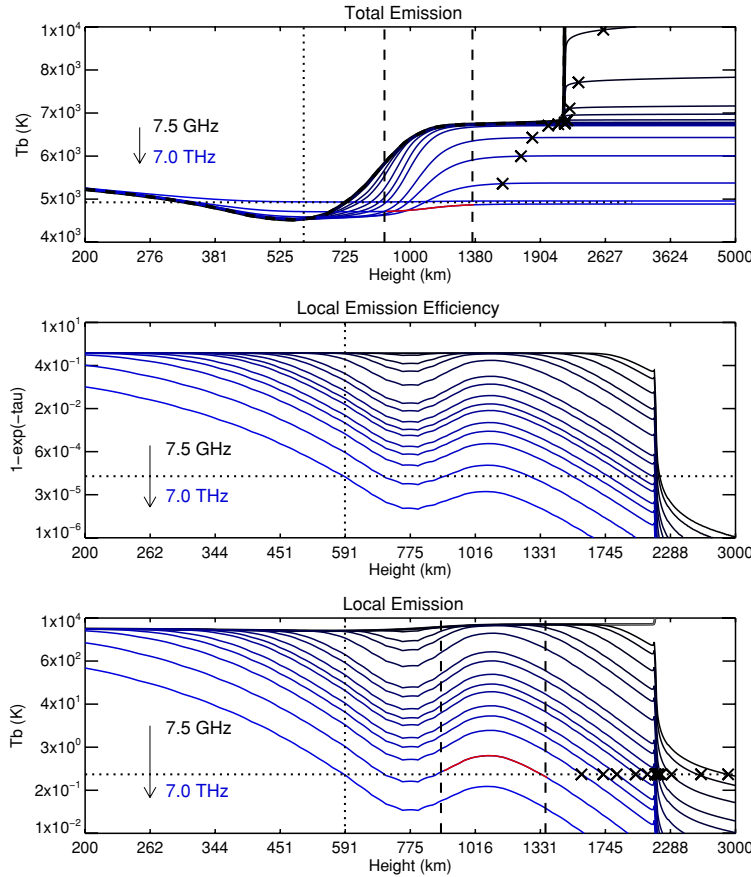
Figure 3. Multi-frequency spectrum from 7.5 GHz (black or upper curve) to 7 THz (blue or lower curve). The total emission (upper panel), "emission efficiency" (middle panel), and local emission (bottom panel) as a function of height from the photosphere. The thick black line in the upper panel is the radial temperature model.
(A color version of this figure is available in the online journal.)

check in the temperature model (the thick line in the upper panel) and see that the temperature model reaches its minimum value MIN(T_R) at h_c. Therefore, by using Equation (8) we are able to obtain the minimal significant emission,

$$I_{\min} < \frac{2k\nu^2}{c^2}\mathrm{MIN}(T_R) \times 10^{-4}, \qquad (9)$$

where MIN(T_R) is the minimum in the atmospheric temperature radial profile.

In order to show the correctness of the previous analysis, in the bottom panel of Figure 3, we have plotted the local emission profiles as a function of height for the same range of frequencies. The horizontal dotted line represents $I_{\min} = 0.44$ K, computed using MIN(T_R) at 7 THz. As expected, this line intersects with the 7 THz profile exactly at h_c.

As an example, we have marked (red line) a non-negligible excess (i.e., above the dotted horizontal line) of local emission at 3 THz, from ∼800 to ∼1300 km of height (marked with vertical dashed lines). And, as shown in the upper panel by a red line in the 3 THz profile, only this excess contributes to the total emission.

For lower frequencies, we have marked with crosses the height where the local emission becomes negligible (that is, where each profile crosses the $I_{\min}$ bound in the bottom panel). This height is also marked with crosses in the total emission profiles (upper panel), showing that the emission at each frequency has already converged to its final value at the marked height.
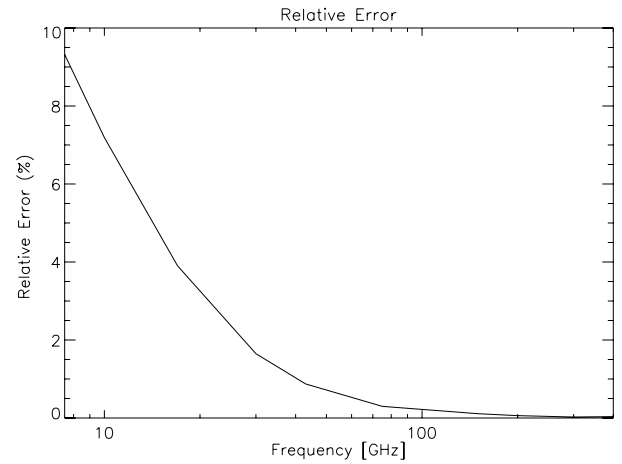

**Figure 4.** Relative error in the final brightness temperature using the min = $I_{\min}$ parameter.

As shown in Figure 4 where we have plotted the error associated with Equation (9), for frequencies higher than ∼40 GHz, the relative error of the final brightness temperature is lower than 1%, whereas for lower frequencies the error is higher, due to the fact that there are large regions (at coronal heights) which contribute with low amounts of local emission.

4. RESULTS

We compute the free–free thermal radio emission from an atmosphere of hydrogen–helium gas, using published (radial)
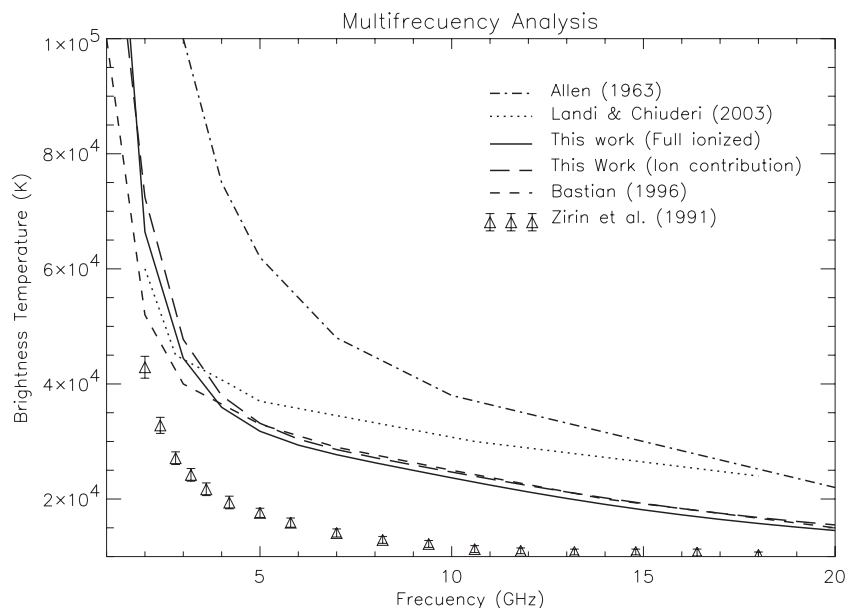
Figure 5. Quiet-Sun brightness temperature as a function of frequency from different models. Triangles show the observations of Zirin et al. (1991).
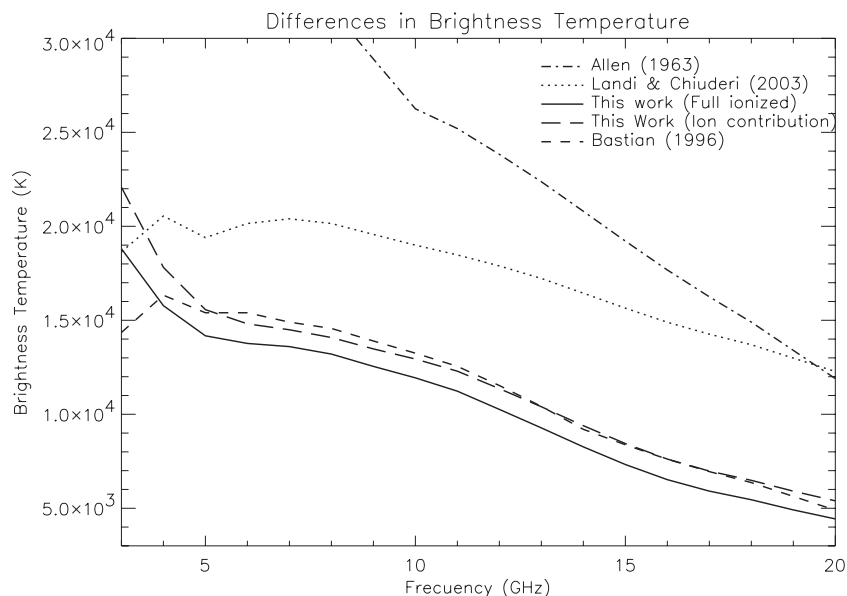
Figure 6. Brightness temperature difference between observations and models as a function of frequency.

profiles of solar temperature and density. We performed a multi-frequency analysis, from 2 to 20 GHz, shown in Figure 5 by continuous and long-dashed lines, and compared our results against observations reported by Zirin et al. (1991; triangles) and similar published analysis. The continuous line is the output of our model using $n_i = n_e$ in Equation (4). The long-dashed line is the output of our model considering radiation from H II, He II, and He III ions in Equation (4). The short-dashed line is the Bastian et al. (1996) model which uses similar physical considerations as our model. The dotted line is the Landi & Chiuderi Drago (2003) model computed from the observed differential emission measure and using an empirical opacity function. We also plotted the Allen (1963; dot-dashed line) model.

In Figure 6, we have plotted the brightness temperature difference, between observations and models, with the same line code as in Figure 5. This difference decreases with frequency.

At ∼5 GHz, our models and Bastian et al. (1996) model have an excess of ∼1.5 × 10⁴ K, whereas the Landi & Chiuderi Drago (2003) model has an excess of ∼2 × 10⁴ K. At ∼20 GHz, all models have better agreement with observations, although the excess computed by our models as well as Bastian et al. (1996) model is only ∼5 × 10³ K.

As our code uses a cellular automaton and an expert system to solve efficiently the radiative transfer equation, we are able to achieve integration times which are up to 1 order of magnitude shorter than direct integration codes (see Appendix B); this makes possible to generate high definition 2D images from 3D structures, in reasonably short times and using very short (1 km) integration steps. Therefore, Pakal can compute the emitting spectrum from highly detailed source structures, as is expected in new generation solar chromospheric models.

We have compared the performance of our code with a similar code published by Selhorst et al. (2005) and with a
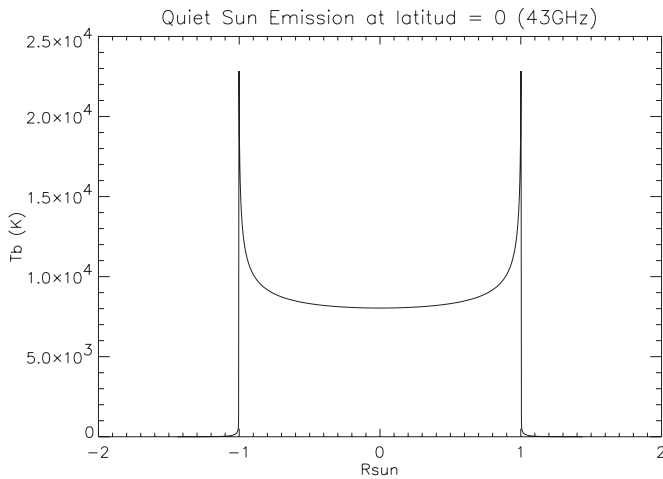
Figure 7. Equatorial cut from the 1024×1024 simulation image of the Sun at 43 GHz. The figure shows the classical limb brightening.

linear integration process (see Appendix B). We found that Pakal can improve the integration time up to 1 order of magnitude compared with the linear integration process and up to 1/3 when compared with the Selhorst et al. (2005) code. We have performed a detailed analysis of the quiet-Sun emission at 17 GHz simulated by Pakal and using temperature and density profiles observed in UV and the continuum (see details in de La Luz et al. 2008).

Figure 7 shows an equatorial cut of a 1024 by 1024 image of the computed quiet-Sun emission at 43 GHz, where the limb brightening is clearly seen. In this case, we used integration steps of 10 km and a minimal local emission of 10^{-17}. We ran the code using the initial values shown in Appendix A. The limb brightening shows a maximum intensity of 23,000 K and a minimum intensity of 8000 K. Observations at similar frequencies, made in the 1950s, reported brightness temperatures from 5700 K to 6000 K at 40 GHz (Whitehurst & Mitchell 1956), although based on later observations at 50 GHz Reber (1971) predicted a higher emission at the center of the disk of 7500 K.

5. SUMMARY

We have developed a new numerical code to solve the radiative transfer equation in a radial (3D) geometry for stellar atmospheres. The code is composed of four independent modules: (1) the numerical model; (2) geometry; (3) numerical methods; and (4) physical stellar models. This architecture allows easy changes when we want to test different physical models.

We found that the minimum of the temperature profile can be used to compute the lower boundary of the emission; this boundary guarantees the numerical convergence of the final brightness temperature.

By improving the geometry and the integration process, the code is able to reproduce, with better results, classical analysis of the solar radio emission, as the analysis of the depth of emission and multi-frequency analysis in 1D or 2D analysis of the limb brightening (Section 4).

The code is up to 1 order of magnitude faster than linear integration codes and 3 times faster than the similar published codes. In the future work, we are going to implement adaptative integration steps and develop the Message Passing Implementation (MPI) of the code which will work in multi processor computers; with these improvements, the code will be able to solve the radiative transfer equation in

nonhomogeneous structures with more complicated physical conditions as non-LTE, more chemical species and emission processes. Finally, the code is free upon request.

APPENDIX A

TESTING THE MODEL

Pakal is able to deal with different opacity functions and chemical species with different ionization states. Although, in order to compare our code with previous published results, we ran the code twice: first, using a restricted initial value of densities, $n_i = n_e$ (as shown by continuous lines in Figures 5 and 6), and second, considering the density of each ionization state of a diatomic gas formed by H–He (long-dashed lines in Figures 5 and 6). The code inputs are as follows.

1. Inputs from libraries:
   a) Source function: the Rayleigh–Jeans approximation (Equation (8)).
   b) Opacity: free–free emission (Equation (6)).
2. Inputs from files:
   a) Radial profiles of temperature, electronic and hydrogen densities: here, we use model C of Vernazza et al. (1981), for chromospheric and low transition zone heights. For coronal heights, we use the Gabriel (1976) model and that reported by Foukal (1990).
   b) Assuming $He = 0.1 * H$.
3. Console inputs: these inputs changed for each particular simulation.

APPENDIX B

ANALYSIS OF CONVERGENCE

The convergence test is necessary when we want to prove the adequate functionality of any code. We have developed three convergence tests, which also help us to test the efficiency of the code. The first one involves the -detail parameter, which determines the length of the integration step when the code is performing a detailed integration process. The second test involves the -min parameter, which sets the minimum emission considered by the code (i.e., emission below this value is neglected). Finally, we analyze the -big parameter, which determines the length of the large integration step used when the local emission is negligible.

In order to set a lower boundary for the minimum emission parameter (-min), we ran several simulations at different frequencies. We found that the -min parameter has non-negligible effects when it is greater than the emission computed at 1% of the minimum of the temperature profile. Note that the final error of the model is associated with this parameter; at least the total error will be comparable to the minimum emission parameter and depends indirectly on the minimum step of integration.

The combination of these parameters determines the efficiency of the code. If we use a very small number for the -detail parameter, the code will take long time for the integration process. On the other hand, the code will loose valuable information by using too large numbers in the -big or -min parameters. Therefore, we need to look for the best parameters in terms of
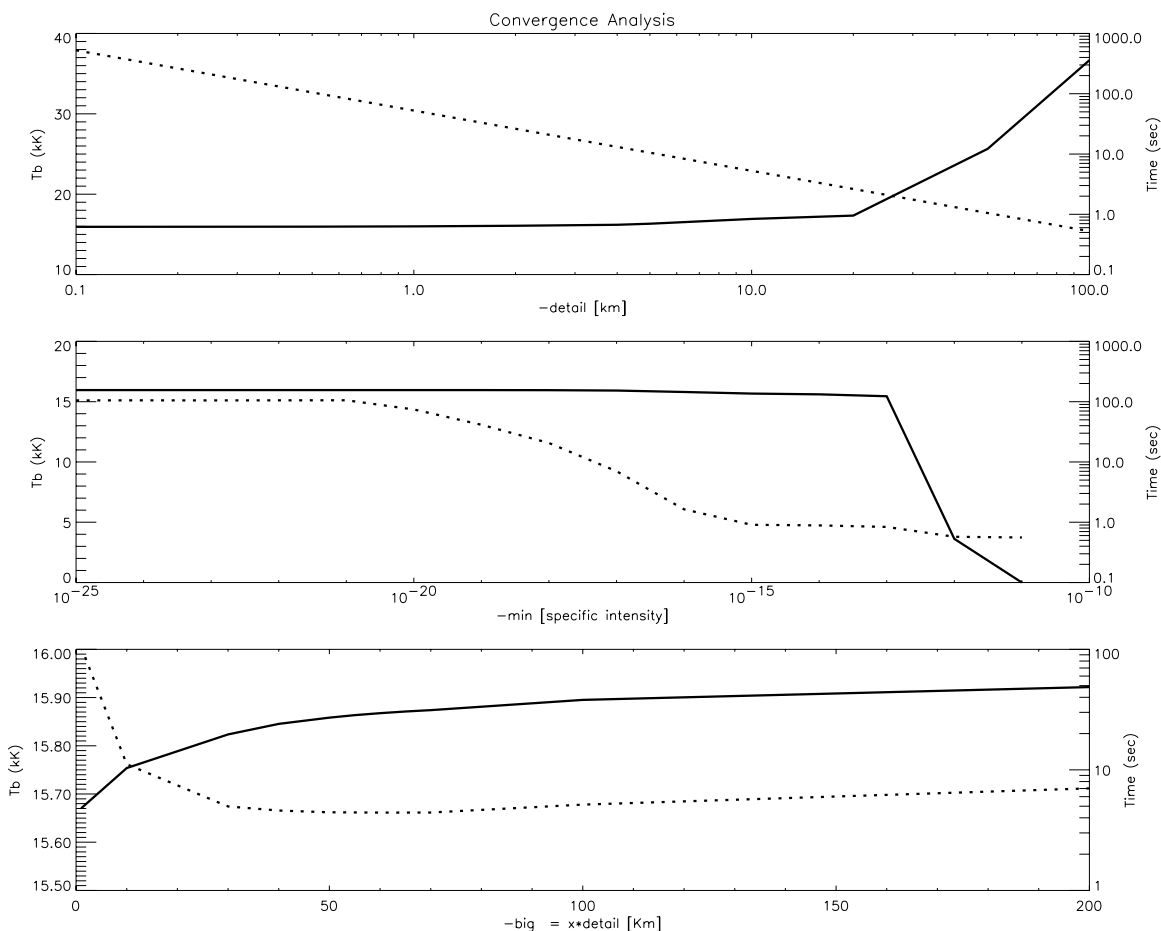
Figure 8. Analysis of convergence of Pakal. The brightness temperature (continuous lines) and the time of the integration process (dotted lines) for the variation of "-detail" (upper panel), "-min" (middle panel), and "-big" (bottom panel) parameters.

the integration time and the stability of the output. In Figure 8, we have plotted the brightness temperature (continuous lines) and the integration time (dotted lines) versus the varying parameters (-detail, -big, and -min, respectively), so we can test the stability and performance of the code. The main idea is to find out the best parameters for the shortest integrations times, but without affecting the final brightness temperature. Those tests were carried out by computing the emission over a ray path in a single pixel at position (0,0), i.e., in the center of the solar disk.

The upper panel of Figure 8 shows the first test, the computed brightness temperature as a function of the small integration step (-detail parameter) using a constant large integration step of 100 km. If we set the -detail parameter to 100 km (i.e., the detail integration and the big integration steps are equal), the resultant algorithm is really poor, because it is integrating sequentially. In this case, the integration time (dotted line in the upper panel of Figure 8) is very fast ($\leqslant 1$ s), but the brightness temperature computed is far away from the right value (1.6×10^4 K). When the detailed integration steps are lower than 20 km, the emission converges to 1.6×10^4 K, although the integration time grows exponentially. For instance, to generate an image of 1024 by 1024 using a small integration step of 10 km, the integration time is almost 2 months. If the small integration step is 1 km, the integration time will be around two years.

To perform the second test, we left both the small (0.5 km) and large (100 km) integration steps constant and allow variations of the minimal emission (-min). The continuous line in the middle panel of Figure 8 shows that the brightness temperature

converges when the minimal emission is lower than 10^{-13}. When the minimal emission is higher than 10^{-13}, the brightness temperature diverges and the integration times are shorter. For instance, if the minimal emission is 10^{-17} and the integration step is 0.5 km, an image of 1024 by 1024 takes 85 days for integration.

In order to find out the best value for both integration steps (third test), in the bottom panel of Figure 8 we have plotted the brightness temperature (continuous line) as a function of the large integration step, in terms of the small integration step (large = $n \times$ small), setting the minimal emission as 10^{-17} and the small integration step as 0.5 km.

Changes of the large integration step do not affect appreciably the brightness temperature, although the integration time is largely affected by such changes. In this case, the integration time may vary in 1 order of magnitude. The minimum time of integration is reached at 60 km (see the dotted line in the bottom panel of Figure 8); this is

$$\text{big[km]} = 60 * \text{detail} = 30 \, \text{km}.$$

Performing the convergence analysis, but using the best parameters, it is possible to obtain integration times which are 1 order of magnitude lower than those in the direct integration process, as shown in Figure 9. For instance, the integration time for a 1024 by 1024 image with small integration steps of 10 km is now 11 days instead of two months. If the small integration step is 1 km, Pakal now takes 39 days instead of 2 years (a super

DE LA LUZ ET AL.
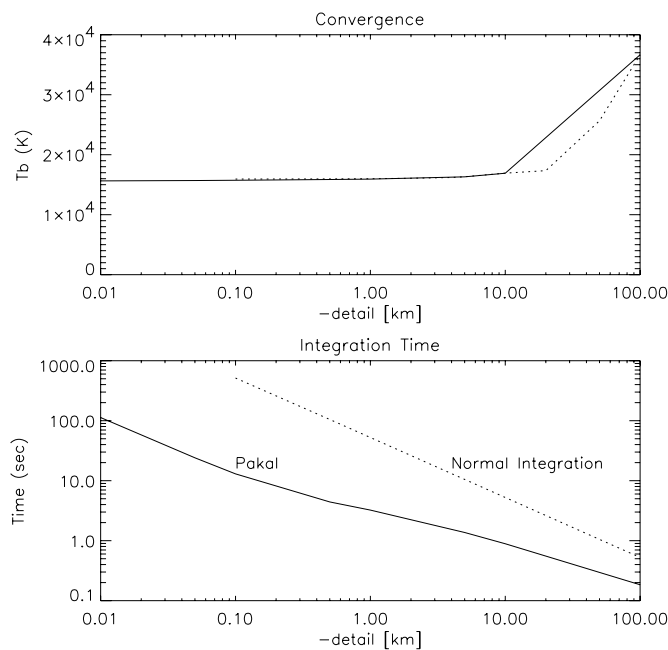
Figure 9. Analysis of convergence of Pakal. The brightness temperature as a function of the short integration steps and the optimal parameters; calling sequence: "./pakal -xy 0 0 -nu 17e9 -min 1e-17 -detail X -big 60." The bottom panel shows the respective time (continuous line) and the time using linear integration (dotted line).

computer with 1024 processors will take 1 hr to generate this image).

We have compared the performance of our code with a similar code published by Selhorst et al. (2005) which practically solves the same task but based on the linear integration method. The border conditions are as follows.

1. Spatial resolution: 1100 points = 770,000 km.
2. Steps of integration: 800.
3. Size of a step: 50 km.

The time results are as follows.

1. Selhorst code: 13 minutes.
2. Pakal code: 33 minutes.

Changing the Pakal integration parameters to the optimal value,

1. detail integration step: 50 km,
2. large integration step: 100*50 km,
3. minimal emission parameter: 1e-20,

we obtain

1. Pakal code: 4 minutes.

In summary, we improved our results by 1 order of magnitude and the linear integration used in another method by 1/3. Even more, that the method used by Selhorst et al. (2005) does not include the computation of the geometry of the problem.

REFERENCES

Allen, C. W. 1963, in IAU Symp. 16, The Solar Corona, ed. J. W. Evans (New York: Academic), 1
Athay, R. G., & Thomas, R. N. (ed.) 1961, Interscience Monographs and Texts in Physics and Astronomy, Physics of the Solar Chromosphere (New York: Interscience)
Bastian, T. S., Dulk, G. A., & Leblanc, Y. 1996, ApJ, 473, 539
Battaglia, A., & Mantovani, S. 2005, J. Quant. Spectrosc. Radiat. Transfer, 95, 285
Behara, N. T., & Jeffery, C. S. 2006, Balt. Astron., 15, 115
Buehler, S. A., Eriksson, P., Kuhn, T., von Engeln, A., & Verdes, C. 2005, J. Quant. Spectrosc. Radiat. Transfer, 91, 65
Cahalan, R. F., et al. 2005, Bull. Am. Meteorol. Soc., 86, 1275
Carlsson, M. 1992, in ASP Conf. Ser. 26, Cool Stars, Stellar Systems, and the Sun, ed. M. S. Giampapa & J. A. Bookbinder (San Francisco, CA: ASP), 499
Cayrel, R., Perrin, M.-N., Barbuy, B., & Buser, R. 1991, A&A, 247, 108
Chandrasekhar, S. (ed.) 1960, Radiative Transfer (New York: Dover)
Davis, A. B., & Cahalan, R. F. 2001, in AGU Spring Meeting Abstracts, (Washington, DC: AGU), 61
de La Luz, V., Lara, A., Mendoza, E., & Shimojo, M. 2008, Geofis. Int., 47, 197
Dere, K. P., Landi, E., Mason, H. E., Monsignori Fossi, B. C., & Young, P. R. 1997, A&AS, 125, 149
Dulk, G. A. 1985, ARA&A, 23, 169
Evans, K. F. 1998, J. Atmos. Sci., 55, 429
Ewell, M. W., Jr., Zirin, H., Jensen, J. B., & Bastian, T. S. 1993, ApJ, 403, 426
Foukal, P. 1990, Solar Astrophysics (New York: Wiley-Interscience), 492
Gabriel, A. H. 1976, Phil. Trans. R. Soc. A, 281, 339
Gustafsson, B., Bell, R. A., Eriksson, K., & Nordlund, A. 1975, A&A, 42, 407
Hauschildt, P. H., Allard, F., & Baron, E. 1999, ApJ, 512, 377
Hillier, D. J., & Miller, D. L. 1998, ApJ, 496, 407
Hubeny, I., & Lanz, T. 1995, ApJ, 439, 875
Iwabuchi, H. 2006, J. Atmos. Sci., 63, 2324
Kurucz, R. L. 1979, ApJS, 40, 1
Landi, E., & Chiuderi Drago, F. 2003, ApJ, 589, 1054
Lyapustin, A. 2002, Appl. Opt., 41, 5607
Oreopoulos, L., Marshak, A., Cahalan, R. F., Várnai, T., Davis, A. B., & Macke, A. 2006, EOS Trans. Am. Geophys. Union, 87, 52
Pauldrach, A. W. A., Hoffmann, T. L., & Lennon, M. 2001, A&A, 375, 161
Reber, E. E. 1971, Sol. Phys., 16, 75
Rohlfs, K. (ed.) 1986, Tools of Radio Astronomy (Berlin: Springer)
Santolaya-Rey, A. E., Puls, J., & Herrero, A. 1997, A&A, 323, 488
Scheirer, R., & Macke, A. 2001, J. Geophys. Res., 106, 14301
Schildt, H. 1987, Lenguaje c: Programacion Avanzada (Berkeley, CA: Osborne/McGraw-Hill)
Selhorst, C. L., Silva, A. V. R., & Costa, J. E. R. 2005, A&A, 433, 365
Shulyak, D., Tsymbal, V., Ryabchikova, T., Stütz, C., & Weiss, W. W. 2004, A&A, 428, 993
Vernazza, J. E., Avrett, E. H., & Loeser, R. 1976, ApJS, 30, 1
Vernazza, J. E., Avrett, E. H., & Loeser, R. 1981, ApJS, 45, 635
Werner, K. 1986, A&A, 161, 177
Whitehurst, R. N., & Mitchell, F. H. 1956, AJ, 61, 192
Zirin, H., Baumert, B. M., & Hurford, G. J. 1991, ApJ, 370, 779